Two-dimensional axisymmetric and three-dimensional helical equilibrium in the line-tied screw pinch

C. Paz-Soldan, M. I. Brookhart, A. J. Clinch, D. A. Hannum, and C. B. Forest

Citation: Phys. Plasmas **18**, 052114 (2011); doi: 10.1063/1.3592998
View online: http://dx.doi.org/10.1063/1.3592998
View Table of Contents: http://pop.aip.org/resource/1/PHPAEN/v18/i5
Published by the American Institute of Physics.

Two-dimensional axisymmetric and three-dimensional helical equilibrium in the line-tied screw pinch

C. Paz-Soldan, M. I. Brookhart, A. J. Clinch, D. A. Hannum, and C. B. Forest
Department of Physics, University of Wisconsin-Madison, 1150 University Avenue, Madison, Wisconsin 53706, USA

(Received 16 March 2011; accepted 3 May 2011; published online 31 May 2011)

The line-tying condition at a conducting anode is shown to provide a localized modification to the well-understood 1-D screw pinch equilibrium in the presence of bulk plasma diamagnetism. Diamagnetic currents cannot flow near the conducting anode and are measured to disappear in a localized boundary layer, causing a weak mirror configuration that breaks 1-D equilibrium and causes large parallel pressure gradients suggestive of significant radial outflows. For sufficiently large plasma currents, the paramagnetic nature of parallel current drives the equilibrium to paramagnetism and destroys the mirror effect. At a critical plasma current, the axisymmetric equilibrium is found to transition to a long-lived, rotating, helical 3-D equilibrium state. Internal measurements of this state via multi-point correlation analysis techniques illustrate that it preserves the flux surfaces and pressure profile of the axisymmetric equilibrium. Measurements indicate that despite the fact that the flux surfaces wander at the anode, the line-tied boundary conditions are not necessarily violated. [doi:10.1063/1.3592998]

I. INTRODUCTION

The 1-D, radial magnetohydrodynamic (MHD) equilibrium of the screw pinch is one of the most fundamental and well understood in magnetic confinement, with thorough treatments in nearly all elementary textbooks.[1] Interest has been renewed in this configuration, however, due to its suitability to the study of line-tied plasma columns. This geometry is relevant to a number of astrophysical systems such as the prominences observed on the surface of the sun[2,3] where MHD instabilities are thought to be a possible cause of solar flares and anomalous coronal heating.[4] The line-tying condition requires the vanishing of electric fields tangent to a perfectly conducting surface, which in the ideal MHD limit corresponds to zero plasma displacement as the plasma is frozen into the magnetic field. Line-tying has been both inferred[5] and mechanically enforced[6] in past experiments using planar and conical conducting anodes, respectively. Conducting anodes have also been shown to provide incomplete line-tying[7] due to finite sheath resistivity at the anode surface.[8] In this study line-tying by a planar anode will be directly measured for certain MHD equilibria. The line-tying condition will be shown to break the assumptions of the canonical 1-D MHD force balance, requiring instead a 2-D equilibrium treatment.

Beyond 1-D and 2-D equilibria, persistent helical states in otherwise axisymmetric systems have been identified in toroidal devices such as RFX-mod,[9] JET,[10] NSTX,[11] and MAST.[12] These persistent states are thought to constitute helical 3-D equilibria, requiring a fully 3-D treatment of MHD force balance. Such states have also been theoretically predicted for straight cylinders[13] and computationally seen,[14] despite the imposition or existence of an axisymmetric boundary condition. This study reports the experimental observation of such a 3-D helical state in the screw pinch.

MHD force balance is given in vector form by:[15]

$$\nabla P = \vec{J} \times \vec{B} - \rho\left(\vec{V} \cdot \nabla \vec{V}\right), \tag{1}$$

where $\vec{V}$ is the plasma flow, ρ is the mass density, $\vec{J}$ is the current density, and $\vec{B}$ is the magnetic field. In the canonical 1-D cylindrical form (only gradients in $\hat{r}$ allowed), Ampère's law $\left(\nabla \times \vec{B} = \mu_0 \vec{J}\right)$ expands Eq. (1) to become in the radial direction:

$$\frac{\partial P}{\partial r} = -\frac{\partial}{\partial r}\left(\frac{B_z^2}{2\mu_0}\right) - \frac{B_\theta}{\mu_0 r}\frac{\partial}{\partial r}(rB_\theta) + \rho\frac{V_\theta^2}{r}, \tag{2}$$

where $V_r = 0$ is assumed, and $B_r = 0$ by necessity. The pressure gradient is supported by the Θ-pinch and Z-pinch term [first and second term on the RHS of Eq. (2)]. The centrifugal term [third term on the RHS of Eq. (2)] is often ignored, though for large enough ρ or V_θ it can lead to a meaningful reduction of the pressure gradient. In 1-D equilibria, the degree of pitch to the magnetic field is parameterized by the safety factor q [$=2\pi r B_z/(LB_\theta)$], where L is the device length. Expanding Eq. (1) into a 2-D equilibrium is achieved by including gradients in $\hat{z}$ which were neglected in Eq. (2), yielding:

$$\begin{aligned}\frac{\partial P}{\partial r} = &-\frac{\partial}{\partial r}\left(\frac{B_z^2}{2\mu_0}\right) - \frac{B_\theta}{\mu_0 r}\frac{\partial}{\partial r}(rB_\theta) + \frac{B_z}{\mu_0}\frac{\partial B_r}{\partial z} \\ &+ \rho\left[\frac{V_\theta^2}{r} - V_z\frac{\partial V_r}{\partial z} - \frac{\partial}{\partial r}\left(\frac{V_r^2}{2}\right)\right],\end{aligned} \tag{3}$$

where axial gradients can thus sustain or degrade the pressure gradient. $V_\theta \gg V_r$ is no longer enforced in Eq. (3), adding an additional term for completeness.

This paper will utilize the canonical 1-D axisymmetric equilibrium of Eq. (2) to describe the bulk plasma. However, it will be shown that the 2-D form of Eq. (3) must be used to

adequately describe a boundary layer at the anode where the line-tying condition generates significant axial gradients. As plasma current is increased, the axisymmetric equilibrium transitions to a rotating, highly coherent, helical state. Though mode onset may be consistent with a current-driven kink mode, the non-linearly saturated state is shown to be a fully 3-D helical equilibrium described by the vector form of MHD force balance given by Eq. (1).

The organization of this paper is as follows: Sec. II introduces the experimental device, the Rotating Wall Machine,[16] and discusses the diagnostics utilized for the present study. Section III details 1-D equilibrium in the bulk plasma, as well as the direct verification of the line-tying condition at the anode and resultant 2-D modifications to the equilibrium. Section IV discusses analysis of coherent fluctuations and their interpretation as a 3-D helical equilibrium present in the device. Section V provides additional discussion of the aforementioned topics.

II. EXPERIMENTAL DEVICE AND ANALYSIS METHOD

The Rotating Wall Machine,[16] shown in Fig. 1, is a screw pinch magnetic geometry with an externally imposed uniform axial guide field ($B_z = 500$ G) twisted by azimuthal fields generated by the plasma current ($I_P = 1$–7 kA). The plasma is formed in a 1.2 m long and 20 cm diameter stainless steel cylinder with an exterior copper liner. The resistive diffusion time (τ_{res}) of the compound wall is 4 ms, while the pulse length is 20 ms. Plasma (hydrogen for this study) is generated by a unique array of 19 washer-stabilized hollow cathode electrostatic current injectors (guns),[17,18] shown in Fig. 1. The discharge begins by striking an arc within the plasma gun nozzle thus creating a high density plasma. The entire gun is then biased with respect to an external anode, injecting space-charge limited currents into the device. Each gun's bias current is independently controlled by a high-speed thyristor-based pulse width modulation system, which allows spatially and temporally varying injected current profiles to be achieved in the device. This system also affords the excellent shot-to-shot repeatability necessary for this study. The plasma terminates on a bullseye-shaped segmented anode. Measurement of the current to each anode ring yields a coarse measurement of the current profile. The anode is constructed of 4 cm thick copper with a τ_{res} of 200 ms, far longer than the discharge duration.

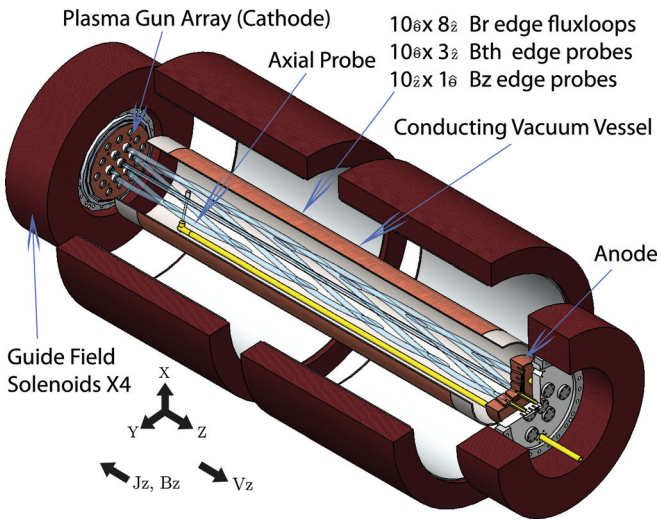

FIG. 1. (Color online) Cross section of the Rotating Wall Machine in the configuration used for this study: The plasma is generated at the plasma source array and is confined by four solenoids. Biasing the source with respect to the anode drives current throughout the discharge forming the screw pinch equilibrium. Qualitatively illustrated discretized plasmas are observed to merge within 1/3rd of the distance to the anode, through a process beyond the scope of this study.

Measurements in the experiment are conducted by a variety of insertable probes and edge magnetic probe and fluxloop arrays. An array of 80 B_r fluxloops (8 axial by 10 azimuthal) surrounds the entire volume of the plasma, and 30 B_θ edge probes are located inside the vacuum vessel at three distinct axial locations. An additional 10 B_z edge probes are spaced equally at one azimuthal location. The guide field solenoids are energized several seconds before the plasma source becomes active, yielding a temporal decoupling of the magnetic fluxes arising from the plasma and from the external solenoids. All internal measurements described in this study are done with an axially inserted probe, also shown in Fig. 1. The probe travels axially on a rail at the edge of the vacuum vessel and can move to any axial location within the vacuum vessel to a precision of 0.5 mm. As the probe head is attached to a 90° articulating joint, rotation of the probe rail allows the probe to sweep a trajectory in the (r, θ) plane through the center of the plasma column. Though this system does not capture full 3-D maps of the plasma column, it does resolve axisymmetric and $m = 1$ phenomena. The probe head itself is interchangeable and for this study Mach, single-tip Langmuir, and tri-axis B-dot probes are used.

Profiles in (r, θ, z) space are built up using extensive shot-to-shot repeatability as the probe is fixed at a single position during a discharge. Figs. 2(a) and 2(c) illustrate a raw, integrated signal from a single B-dot probe coil at a certain spatial location, along with 1 ms-bin time average values. As shown, even discharges with strong fluctuation levels have well-defined mean values from which radial profiles can be created. As all components of $\vec{B}$ are measured [shown in Figs. 2(b) and (d)], a direct measurement of the axial and azimuthal (approximately the parallel and perpendicular) currents using Ampère's law as well as the local value of the safety factor q is possible. Using Eq. (2), local spatial gradients in $\vec{B}$ are related to the plasma pressure gradient which is then integrated to calculate a radial pressure profile. This integration is carried out from the plasma edge to the core from each direction, allowing a rough gauge of the error by noting the degree of core pressure mismatch. Pressure integration is valid for time scales longer than the Alfvén time τ_A (≈ 2 μs), a condition easily met by the 1 ms time binning utilized.

III. AXISYMMETRIC EQUILIBRIUM

A. High-q diamagnetic equilibrium

Weakly biasing the plasma guns ($I_{discharge} > I_p$) generates a strongly diamagnetic, high q ($\approx$3–4) plasma in which the pressure gradient is primarily supported by the $\frac{\partial}{\partial r}\left(\frac{B_z^2}{2\mu_0}\right)$

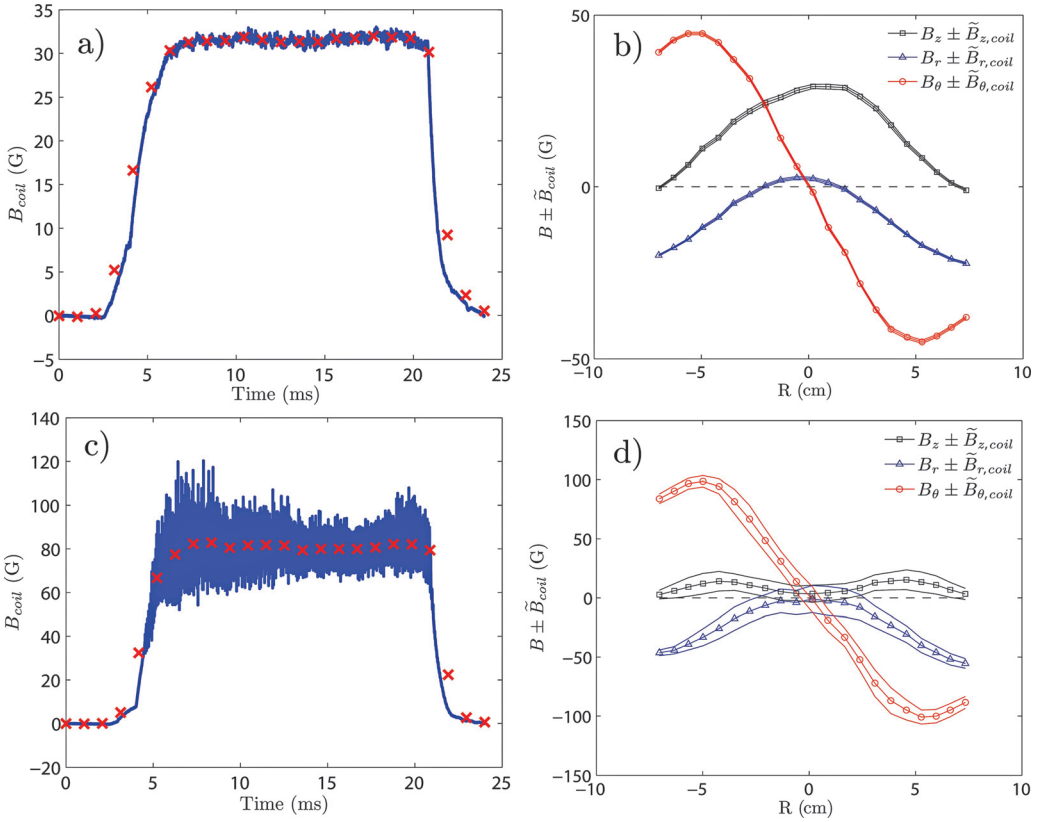

FIG. 2. (Color online) Raw (integrated) signal from the B-dot probe under (a) quiescent and (c) fluctuating conditions. The crosses are 1 ms-bin time-averages of the signal, which are well-defined despite the large fluctuations present. Radial profiles of 1 ms-bin time-averages are displayed in (b) for the quiescent and (d) for the fluctuating case, along with the relative fluctuation amplitude, illustrating the ability of shot-to-shot repeatability at the millisecond level to resolve well-defined spatial information.

term of Eq. (2), as shown in Fig. 3. Equivalently, the contribution to $J_\perp$ is primarily from J_θ over J_z. This indicates that the equilibrium is Θ-pinch like, and as such is robustly stable to MHD instabilities. The large diamagnetism ($\delta B_z \equiv B_{z,guide} - B_{z,observed} < 0$) also lowers the q profile by reducing the local B_z, and this effect can be significant at weak guide fields. The magnitude of the pressure gradient is also large, yielding a core β ($\equiv \frac{2\mu_0 P_0}{B_z^2}$) of 15%, illustrating that the usual force-free approximation used to describe screw-pinch equilibria is not applicable to this plasma. The absence of a force-free current profile can be easily understood by noting that though the current profile is stationary in time, it is strongly sourced and sinked by the guns and anode, respectively.

B. Two-dimensional equilibrium and anode mirroring

The large δB_z of the high-q equilibrium shown in Fig. 3 also allows a unique and direct confirmation of anode line-tying to be performed. At the highly conducting anode surface, any ΔB_z in time interval $\Delta t < \tau_{res}$ is forbidden as the line-tying condition requires $E_t = 0$. It would thus be expected that $\delta B_z = 0$ at the anode surface, leading to a weak magnetic mirror. Experimental observations, shown in Fig. 4, clearly display this behavior, though measurements at the exact surface of the anode are impossible due to finite probe size. This constitutes a direct measurement of magnetic fieldline tying in a plasma by a conducting anode and illustrates that its effects are highly localized. This scale length is set by the competition between advection and diffusion of the magnetic field as axial flows (V_z) present in the device tend to advect field perturbations downstream while diffusion allows perturbations to move upstream. The parallel magnetic field diffusion coefficent ($D = \eta/\mu_0$) using a past measurement[19] of η is 120 m^2/s. From the induction equation, $D \approx (\Delta Z) V_z$, where measured $V_z \approx 6$ km/s sets a scale length (ΔZ) of ≈2 cm, consistent with the observed scale length.

The nature of MHD radial force balance is significantly altered in a narrow anode boundary layer (ABL) as the dominant contribution to Eq. (2) [the $\frac{\partial}{\partial r}\left(\frac{B_z^2}{2\mu_0}\right)$ term] is much reduced. This requires a transition from the 1-D form of Eq. (2) to the 2-D form of Eq. (3) in the ABL. To analyze the 2-D equilibrium in this region, measured plasma parameters are presented in Fig. 5. The B-dot probe is capable of directly measuring the magnetic field terms of Eqs. (2) and (3), and results are shown in Figs. 6(a)–6(c). Measurements at Z = 115 cm are in the bulk plasma, where Eq. (2) is expected to hold, while measurements at Z = 121 cm are partway into the ABL, and the anode is at Z = 123 cm. The reduction in δB_z leads to a large reduction in the $\frac{\partial}{\partial r}\left(\frac{B_z^2}{2\mu_0}\right)$ term in the ABL. This imbalance must be compensated for by other terms in Eq. (3). The $\frac{B_\theta}{\mu_0 r}\frac{\partial}{\partial r}(rB_\theta)$ term is unaffected by the transition into the ABL. The $\frac{B_r}{\mu_0}\frac{\partial B_z}{\partial z}$ term, not present in Eq. (2), is present in the ABL, but is insufficient to account for the force imbalance in the

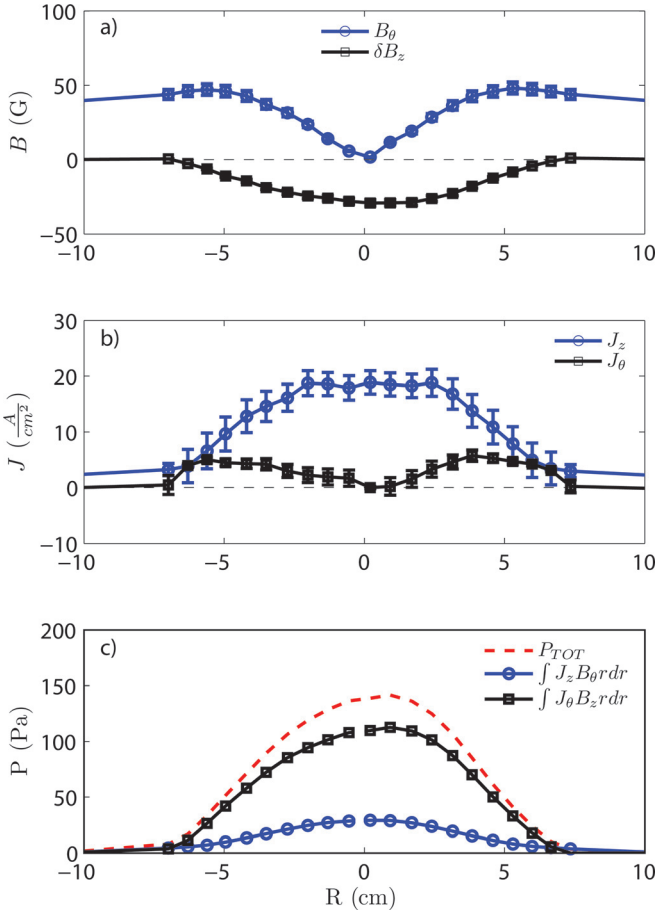

FIG. 3. (Color online) 1-D screw-pinch equilibrium under a low plasma current operation, illustrating the strongly diamagnetic nature of the equilibrium. (a) δB_z is the perturbation to the axial guide field by (b) currents internal to the plasma. (c) The pressure gradient is supported primarily by diamagnetic currents, with the resultant equilibrium similar to that of a Θ-pinch. The boundary condition is provided by edge probe array measurements.

ABL. Thus, the total magnetic body force is reduced and must be compensated for by either reducing the pressure gradient or generating large flows or both.

An approximate analysis is carried out in the ABL by first neglecting the flow terms of Eq. (3) and integrating the

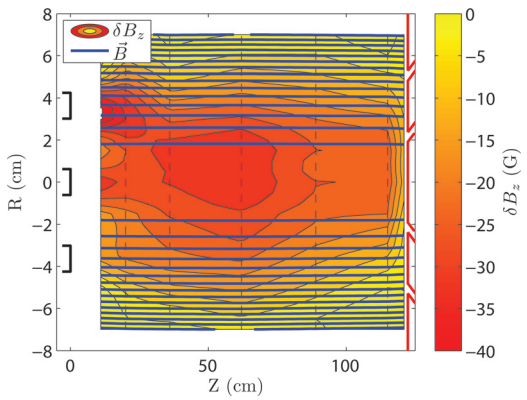

FIG. 4. (Color online) The perturbation to the guide field (δB_z) by diamagnetic currents exists throughout the bulk of the plasma. Near the anode, the line-tying condition prevents δB_z from penetrating. The scale length of this phenomena is seen to be ≤ 5 cm, the resolution of which is limited by the finite axial spacing of the probe sweeps. Due to the strong guide field, field-line deflection is not large, though a weak magnetic mirror results. Dashed lines indicate the axial location of probe sweeps of 21 radial points.

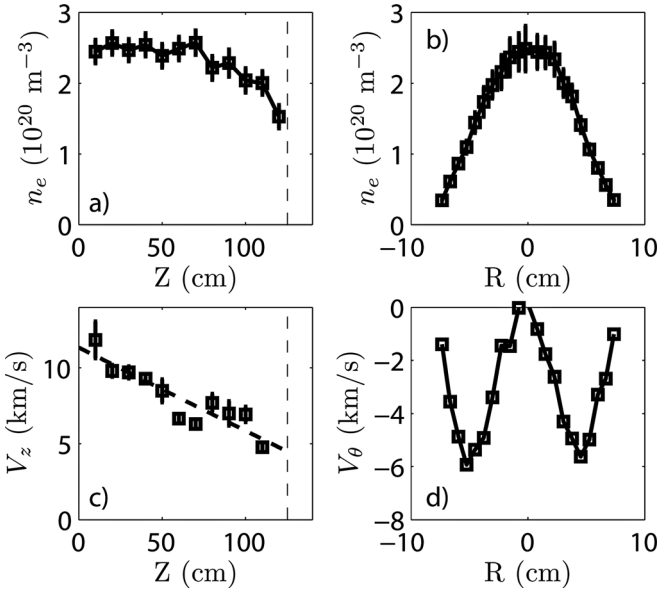

FIG. 5. Profiles of key plasma parameters in the device. Plasma density n_e (measured using ion saturation current to an electrostatic probe) is found to be large and collimated radially, with weak variation axially until near the anode. T_e is measured to be uniformly 3.5 ± 0.5 eV (not shown) using a single-tip Langmuir probe. The cathode (plasma gun face) is at Z = 0 cm, while the anode is at Z = 123 cm and is indicated by dashed lines. V_z is measured using a Mach probe head. A monotonic slowing down is seen as the plasma traverses the column. The physical mechanism of the flow and its axial profile is beyond the scope of this study. V_θ is the $_E \times B$ motion inferred from plasma potential gradients measured by the single-tip Langmuir probe. Radial profiles are made at the midplane while axial profiles are at the geometric axis.

resultant pressure profile (P_{MHD}), shown in Fig. 6(c). For the bulk plasma, P_{MHD} is a very good approximation to the true pressure as V_r, $B_r = 0$ is expected and the inferred values of V_θ from $E \times B$ drifts[16] [Fig. 6(d] indicate that the $\rho \frac{V_\theta^2}{2}$ term is negligible at the anode. For the ABL, it is not possible to a priori neglect the V_r terms, though as they contribute to sustaining the pressure gradient; the Z = 121 cm P_{MHD} profile is thus a lower limit, though it is consistent with the decrease of n_e shown in Fig. 5(a). P_{MHD} thus exhibits a strong parallel pressure gradient and loss of plasma particles from Z = 115 cm to 121 cm. As T_e is measured to be spatially uniform, the spatial variation in P_{MHD} arises from density gradients and these gradients are used to calculate the V_r necessary to satisfy the incompressible continuity equation without particle sources or sinks, where V_z is measured [shown in Fig. 5(c)]. This limiting case V_r is then used to compute the remaining flow terms in Eq. (3), which are shown to be small [Fig. 5(f)]. As the P_{MHD} profile utilized is a lower limit and as V_r arises from this pressure decreases, the V_r limit is thus an upper one and the neglect of the flow terms is thus justified in the original approximation. Confirmation of these estimates naturally requires a direct measurement of the radial flow (V_r) profile, as the assumption of incompressibility may be inaccurate. Particle sources and sinks, however, are not thought to play an important role as the mean free paths of ionization and recombination are much larger than the spatial scales relevant to the ABL. Furthermore, measurements are limited to Z = 121 cm by the spatial scale of the probe. It is expected that the force imbalance of Fig. 5(a) will become more pronounced closer to

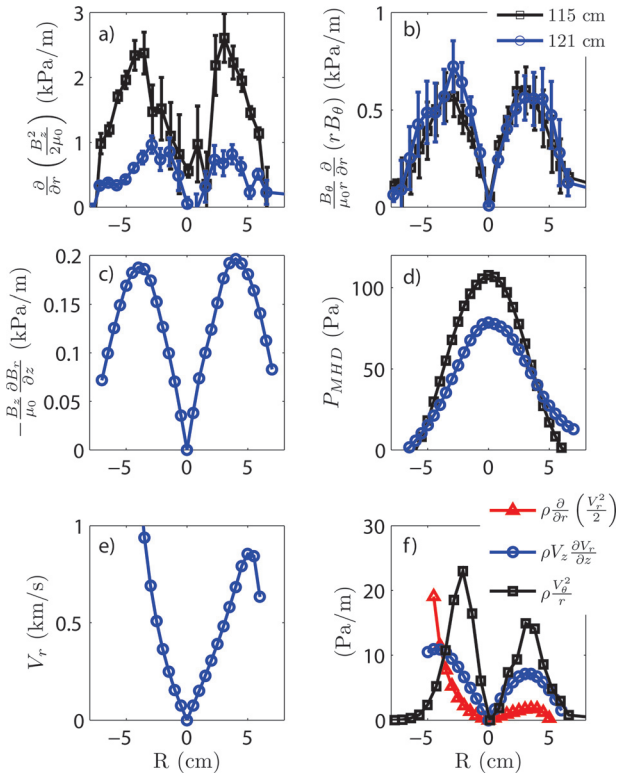

FIG. 6. (Color online) Analysis of Eq. (3) in the boundary layer where the line-tied condition breaks the 1-D form of radial MHD equilibrium. Measurements at Z = 115 cm are in the bulk plasma region, where Eq. (2) is expected to hold, while measurements at Z = 121 cm are partway into the anode boundary layer, and the anode is at Z = 123 cm. (a) The diamagnetic term is much reduced in the boundary layer while (b) the Z-pinch term is unaffected. (c) The 2-D nature introduces a new term into radial force balance. (d) Pressure profiles from the integration of the $J \times B$ forces illustrate the reduced pressure from the weakened diamagnetic term, which is partially offset by the new axial term. (e) Radial flow V_r approximated from the incompressible continuity equation using the P_{MHD} profiles. (f) The remaining flow terms of Eq. (3) using the V_r of (e) are shown to be small.

the anode, leading to larger axial gradients. It is further speculated that the observed lack of density pile-up at the anode despite the large V_z is due to the pumping effect of V_r. If particles retain radial momentum after recombination, neutral and plasma particles alike would be driven into expansion volumes at the anode end.

C. Transition to paramagnetic equilibrium

As more $J_{||}$ ($\propto I_P$) is injected into the plasma by increasing the bias voltage on the plasma guns, the diamagnetic equilibrium transitions to paramagnetism and the anode boundary layer effect is lost. This is because the magnetic field unit vector exhibits a greater pitch thus giving a solenoidal component to $J_{||}$ and contributing positive (paramagnetic) δB_z to the core. This effect is counter to the J_θ currents produced by the plasma gun itself. Thus, increasing I_P transitions the core plasma from diamagnetic to paramagnetic in nature, and eliminates the anode mirror effect described in Sec. III B. The nature of the canonical 1-D radial MHD-force balance of Eq. (2) is also altered by the paramagnetic effect, with the $J_z B_\theta$ drive becoming dominant over the $J_\theta B_z$ term, as shown in Fig. 7. This geometric effect is well known[20] but

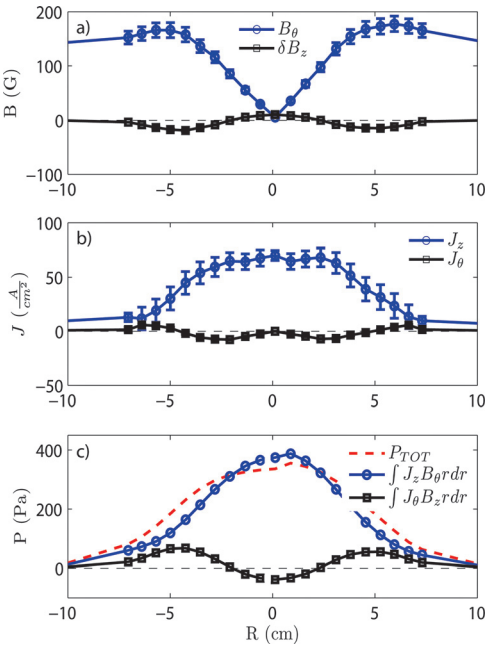

FIG. 7. (Color online) 1-D equilibrium magnetic fields during high current operation. (a) The diamagnetism is shown to be greatly reduced in this case as (b) increasing $J_{||}$ is strongly paramagnetic. (c) The pressure gradient is primarily balanced by gradients in B_θ, unlike the low current discharge of Sec. IV A, and the resulting equilibrium is Z-pinch like.

is rarely demonstrated experimentally due to the fact that $\delta B_z \ll B_{z0}$ in most devices.

D. Confinement scaling of axisymmetric equilibria

Figure 8 illustrates that increasing the plasma current (I_P) and guide field (B_z) found to both lead to higher core pressure (P_0) though differing effects on $\beta = \langle P \rangle / (B_z^2/2\mu_0)$ are seen. The large amount of Ohmic heating from $I_P \propto J_{||}$ results in a very high value of β, both in a peak and volume averaged sense. A linear dependence of volume-averaged β on I_P is seen, though Ohmic power $P \propto \eta I_P^2$ (where η is the resistivity and is $\propto T_e^{-\frac{3}{2}}$) and measurements indicate T_e and thus η are insensitive to I_P. This is reconciled by noting that for open ended devices, particle flux Γ (and thus power loss) is overwhelmingly directed to the end plates giving $\Gamma \propto n_e C_s$, where C_s is the sound speed and is $\propto T_e^{\frac{1}{2}}$. Past measurements[16] have shown that $n_e \propto I_P$, while T_e is insensitive to I_P. Thus, while $P \propto I_P^2$, $\Gamma \propto I_P$, resulting in the observed $\beta \propto I_P$ scaling. In the limit of zero I_P (unbiased plasma), the plasma guns still produce plasma, which leaks along the guide field while maintaining ambipolarity yielding the finite β values observed. Core β deviates from linearity with I_p due to diamagnetism significantly modifying B_z in the core. Guide field scaling ($B_z \propto \langle P \rangle$) illustrates that reduced Larmor radii are effective in increasing confinement even in open ended devices, though the B_z^{-2} dependence in the definition of β yields a $\beta \propto B_z^{-1}$ final β scaling.

IV. HELICAL EQUILIBRIUM STATE

The lower q (≈1–2), higher (I_P) equilibria discussed in Sec. III C are also characterized by the appearance of

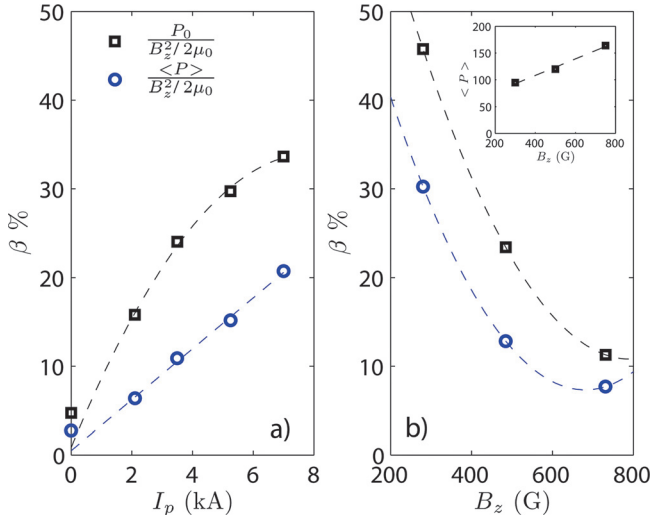

FIG. 8. (Color online) Scaling of peak and volume averaged plasma $\beta = P/(B_z^2/2\mu_0)$ with plasma current I_P and guide field B_z. The plasma created by the plasma gun array is exceptionally high β, due to the large amounts of Ohmic power (up to 1 MW) deposited in the bulk plasma. (a) A linear dependence on I_P is seen for volume averaged β which breaks down in the limit of zero I_P, while diamagnetism in B_z breaks this trend for core β. (b) $B_z \propto P$ as B_z increases confinement, though the B_z^{-2} dependence in the definition of β yields a $\beta \propto B_z^{-1}$ final scaling. Simple trendlines are also shown. P_0 and $\langle P \rangle$ are computed by integrating the 1-D radial force balance of Eq. (2).

long-lived coherent fluctuations in the magnetic and kinetic profiles. Typical magnetic field measurements for this mode are shown in Fig. 9. It is exceptionally coherent and dominantly m = 1 with a helical twist. The mode is global, but with the largest amplitudes observed at the anode end. It is also a global mode of the device with a single frequency

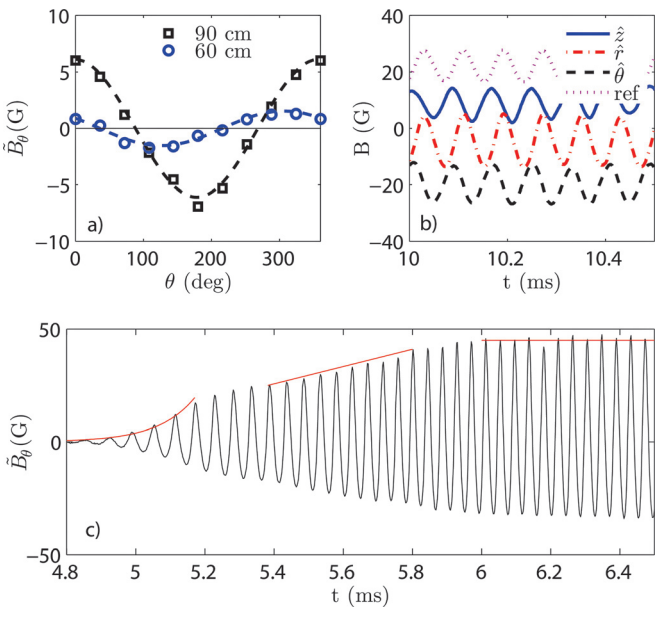

FIG. 9. (Color online) (a) Edge B_θ probes illustrate the presence of an m = 1 perturbation that has a helical twist. (b) B-dot probe signals illustrating the exceptional coherence and single-harmonic structure of the fluctuation. The directions of the signals refer to the probe frame, which is distinct from the cylindrical frame as seen in Fig. 1. An edge B_θ probe is also shown (ref), which is used as a clock to correlate signals from separate discharges and build up internal profiles as discussed in Sec. IV B. (c) High-pass filtered edge B_θ coil illustrates that onset of the perturbation is characterized by an exponential growth phase, followed by a linear growth phase indicating nonlinear interactions, until a saturation amplitude is reached.

present throughout. Detailed internal measurements illustrate that mode is a helical equilibrium state, as will be discussed in the following sections.

A. Scaling and onset

Coherent mode scaling with I_P and B_z is complex, as shown in Figs. 10(a)–10(d). Onset occurs at a critical plasma current I_P (equivalent to a critical $J_{||}$), though this critical current is seen to vary weakly with the axial magnetic field B_z. This is inconsistent with a critical safety factor (q) for excitation expected by external kink theories.[21,22] Furthermore, the mode can be excited by increasing the guide field (B_z), which would tend to be stabilizing to the external kink mode. The current profile is modified and becomes somewhat more peaked as B_z is increased, but measurements using the segmented anode (not shown) indicate that the $q \propto B_z$ nonetheless. The frequency of the mode is increased as I_P or B_z is increased, but this dependence is weak with B_z. The growth rate (γ) for the mode in the exponential phase [shown in Fig. 9(c)] is found to be in the 6–10 kHz range. A weak $\gamma \propto I_P$ scaling is observed, while no dependence on B_z is seen. As the experimental scatter in γ is great due to the short duration of the exponential phase, no analysis of this scaling is presented.

The observed mode frequency (f_{mode}) at a single coil is simply that of the Doppler shift of the rotating m = 1

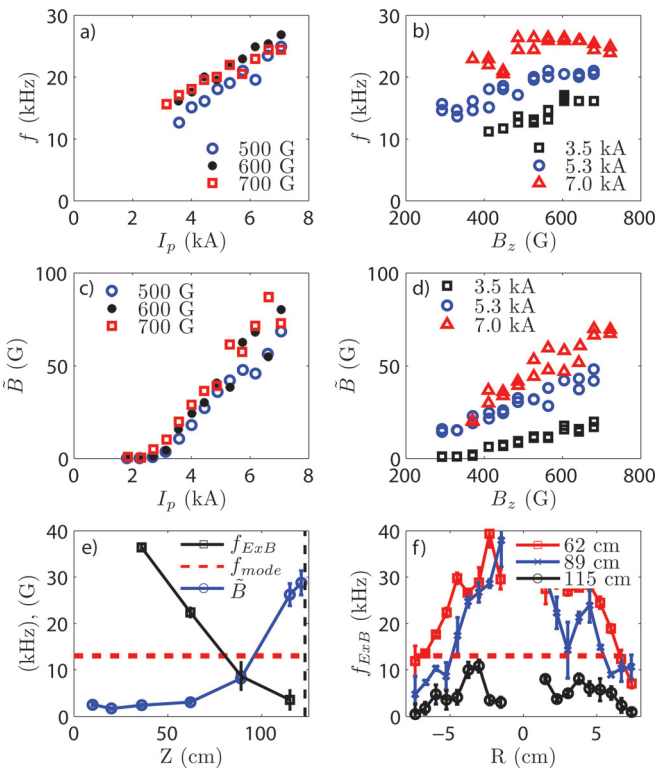

FIG. 10. (Color online) (a) The coherent mode of Sec. IV is shown in (a) to linearly increase in frequency as plasma current (I_P) is increased. (b) Frequency dependence on B_z is increasing at lower I_P but static at higher I_P. (c) Mode amplitude ($\tilde{B}$) increases linearly with I_P, and the critical current for excitation is not found to occur at a single value of safety factor q. (d) $\tilde{B}$ also counter-intuitively increases with increasing B_z. (e) Axial structure of the $E \times B$ frequency and $\tilde{B}$ for the 500 G, 3.5 kA case. Mode amplitude is largest where $f_{mode} < f_{ExB}$. (f) Significant radial shear in f_{ExB} also exists, requiring a mode-weighted volume average to relate f_{ExB} to f_{mode}.

perturbation. f_{mode} is large enough that the conducting vacuum vessel appears ideal and thus $\tilde{B}_r = 0$ at the wall. Analysis discussed in Sec. IV B will show that the typical radial scale size of the oscillation is ≈ 5 cm, which allows conversion from f_{mode} (13 kHz for the Sec. III B case) to a mode azimuthal velocity (v_{mode}), which is found to be ≈ 4 km/s, and directed in the $E \times B$ direction. This velocity is sub-Alfvénic and subsonic as these speeds are ≈ 75 and 25 km/s, respectively.

Figure 10(e–f) illustrates that an axially and radially sheared $E \times B$ flow (v_E) profile likely exists in the device, as radial electric fields (E_r) are measured[16] without significant radial currents thus requiring $v \approx v_E$ to balance Ohm's law. Despite the sheared v_E profile, a single, global f_{mode} is observed, shown by the dotted lines in Figs. 10(e)–10(f). Though the process by which a global mode frequency is selected in a sheared flow is relatively unexplored analytically and computationally, it can be intuitively inferred that a volume-weighted average is taken to select the mode velocity. With this hypothesis, scaling with I_P is easily understood as $v_E \propto E_r \propto E_z \propto I_P$, though scaling with B_z is more complex. Mode axial extent increases towards the cathode with increasing B_z (and I_P) and begins to inhabit regions of larger v_E. Thus, as the volume-weighting includes regions of larger v_E, larger frequencies would be observed, consistent with observations. Mode amplitude is the largest when $v_{mode} > v_E$, indicating that v_E may be setting the axial scale size of the mode in addition to its frequency.

B. Internal analysis

The exceptional coherence of the raw magnetic signals [samples shown in Figs. 2(a), 2(c), and 9(b)] allows the use of a reference signal (an edge B_θ coil) to clock signals across different discharges, thus enabling internal profiles of the fluctuating field to be constructed. Each magnetic field component has a well-defined phase shift (δ_ϕ) from the reference signal, and δ_ϕ can be measured at different spatial locations. In this way, utilizing shot-to-shot repeatability, radial and axial profiles of δ_ϕ can be obtained, as shown in Fig. 11(b). A fast Fourier transform (FFT) based algorithm is used, as cross-correlation techniques are unnecessary due to the dominantly single-mode time-dependence. Mode amplitudes are trivially extracted from the FFT, as shown in Fig. 11(a).

Full 3-D maps of each component of the fluctuating magnetic field can be constructed using the decomposition,

$$\tilde{B}(r,\theta,z,t) = \tilde{B}(r,z)\cos\left(\omega t - m\theta - \delta_\phi(r,z)\right), \qquad (4)$$

where global mode frequency (ω) is taken to be an average for all discharges in the series ($\delta\omega/\omega \approx 2\%$ over the > 100 discharges used to create a map). The azimuthal mode number (m) is taken to be 1 throughout the profile based on edge measurements by the B_θ array shown in Fig. 9(a). The phase shift (δ_ϕ) is also a function of probe position and desired component, as is the fluctuation amplitude ($\tilde{B}$). As all parameters in Eq. (4) are known, the 3-D (r,θ,z) space can be populated. For the following measurements, the measurement grid is 5–7 axial locations by 11 radial locations, corresponding to a spacing of ≈ 20 cm and 5 mm, respectively.

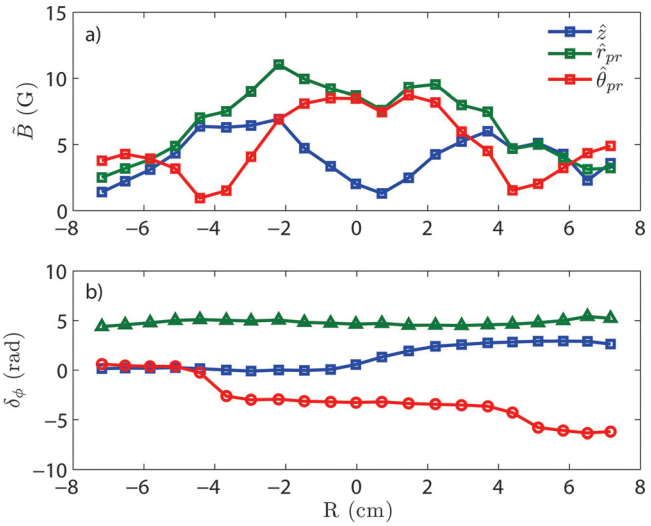

FIG. 11. (Color online) Using an edge B_θ signal as a reference (or click), relative phase shifts from different discharges can be directly compared and radial profiles built of both fluctuation amplitude ($\tilde{B}$) and relative phase (δ_ϕ) using simple FFT based algorithms. This method relies on the exceptional coherence of the signals and on the shot-to-shot reproducibility of the discharge.

The 3-D fields constructed using Eq. (4) illustrate that the mode is global in nature, existing throughout the plasma core and with significant internal structure. All parameters are decomposed into mean-field and fluctuating components, using the notation $\vec{B} = B_0 + \tilde{B}$. Ampère's law is similarly decomposed, with Figs. 12(a) and 12(d) illustrating fluctuating contributions and Figs. 12(b) and 12(e) illustrating total, instantaneous fields. The fluctuating axial current $\tilde{J}_z$ exhibits a peak at r = 5 cm, which when summed to the equilibrium J_{z0} causes a rigid shift in the current channel, shown in Figs. 12(b) and 12(d). Time dependence is a simple rigid rotation of the fluctuating profiles shown in Figs. 12(a) and 12(b).

As $1/\tau_A \ll \omega$, radial MHD force balance is still upheld throughout the oscillation. Equation (1) is also decomposed into mean-field and fluctuating components, yielding

$$J_0 \times B_0 + J_0 \times \tilde{B} + \tilde{J} \times B_0 + \tilde{J} \times \tilde{B} = \nabla P + \nabla \tilde{P}, \qquad (5)$$

where flow has been ignored as measurements are taken away from the anode boundary layer of Sec. III B. As shown in Figs. 12(c) and 12(f), summing all terms in Eq. (5) yields a force profile that is dominantly radial, while each individual contribution from Eq. (5) is not. Furthermore, the force null is now offset from the geometric axis of the device. The contribution to this perturbed force profile is equally shared between the second and third terms of Eq. (5) and the Maxwell stress is found to be vanishingly small due to fluctuation coherence. This is also true of the Hall dynamo term in Ohm's law. This force profile can be integrated and generally circular pressure contours are found, shown in Figs. 12(c) and 12(f). As with Figs. 12(b) and 12(e), a rigid shift is seen of the pressure maximum. Thus, the fluctuating currents and fields act to offset the plasma centroid while maintaining its overall structure. Figure 13 illustrates using fieldline mapping that the flux surfaces are also maintained throughout the plasma, consistent with equilibrium being maintained. The

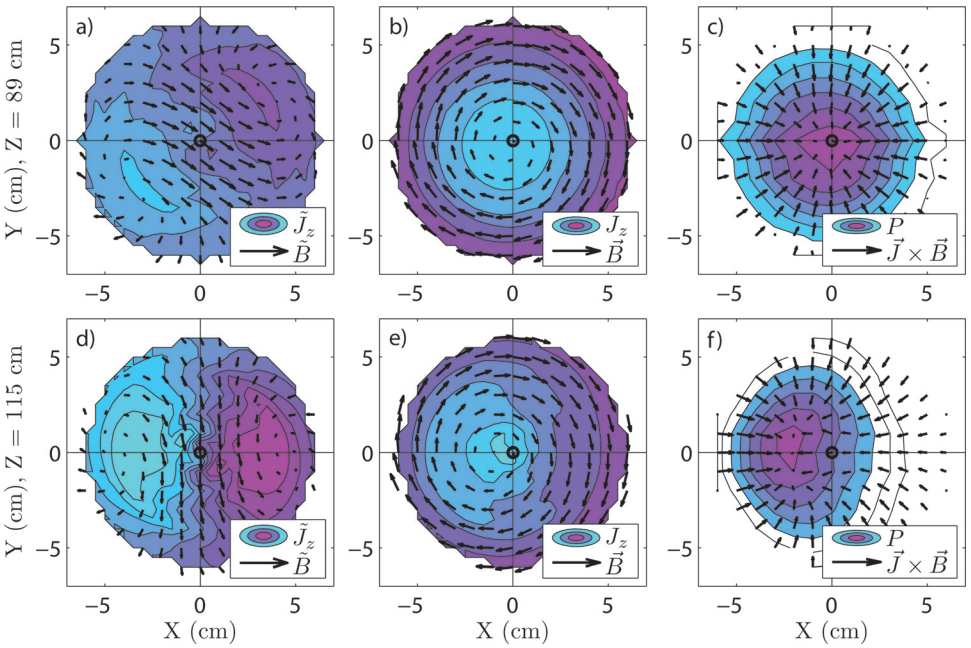

FIG. 12. (Color online) Fluctuating and total contributions to Ampère's Law and radial MHD force balance for the helical equilibrium state at two axial locations to indicate the helical twist. (a) and (d) illustrate the fluctuating fields leading to a rigid shift in the current centroids, shown in (b) and (e). Integrating $\vec{J} \times \vec{B}$ also indicates the pressure centroid is shifted, shown in (c) and (f). All parameters are decomposed into mean-field and fluctuating components, using the notation $\vec{B} = B_0 + \tilde{B}$.

flux surfaces are also seen to be offset at the anode and are found to trace a circular pattern around the geometric axis. The validity of the line-tying condition in this context will be discussed in Sec. V.

V. DISCUSSION

The direct observation of the line-tying of magnetic fieldlines by a conducting anode discussed in Sec. III B is in contrast to other results in which sheath resistance is found to break the line-tying condition at a conducting boundary.[7,23] This not inconsistent with a recent theory[8] as the non-dimensional κ parameter [Eq. (49) in Ref. 8] which gauges the importance of sheath resistance (where $\kappa \gg 1$ indicates strong sheath effects) is found to be ≈ 0.05 as opposed to $\kappa \approx 15$ cited for an experiment in which significant sheath effects are observed.[7,23] Physically, this corresponds to a lower total sheath resistance due to larger plasma density and consequently smaller sheath axial dimensions (electron and ion Debye lengths are 0.2 and 0.9 μm, respectively).

As with the axisymmetric case, a dramatic reduction in $\widetilde{B_z}$ and δB_z very near the anode is observed for the helical equilibrium of Sec. IV. In contrast, $\tilde{B}_{r,\theta}$ reaches its maximum amplitude at the anode, a result which (in addition to an off-axis emissivity maximum) has been previously interpreted as imperfect line-tying.[6,24] Although measurements reported in this study do not preclude imperfect line-tying, an alternate explanation that maintains the line-tying boundary condition yet allows fieldline (and thus flux surface) wandering is presented. As discussed in Sec. III B, the flux surfaces are seen to trace out a circular motion with a radial excursion of ≈ 1 cm. However, as $\widetilde{B_z} \approx 0$ at the anode, the flux surfaces are no longer helical as they were in the bulk plasma but are normal to the anode surface. In the presence of axial flow, plasma sourced at the cathode will follow the flux surface trajectory until it strikes a point on the anode consistent with the flux surface strike point. Flux surface and plasma tangential excursions from their upstream (cathode) launch point are thus the result of perturbations in the bulk plasma due to the helical equilibrium state. At a later time, a different mapping takes place, and plasma sourced at the same upstream launch point will strike a different location of the anode, but again with velocity and current purely normal to the anode surface. Between these two instants in time, the apparent motion of the flux surface can be mistaken to be a tangential velocity though in fact what is being observed is time-dependence in the normal component, which does not violate the line-tying condition. Notwithstanding, as E_t is not measured at the anode surface, existing measurements cannot conclusively determine if line-tying is upheld in the helical equilibrium state.

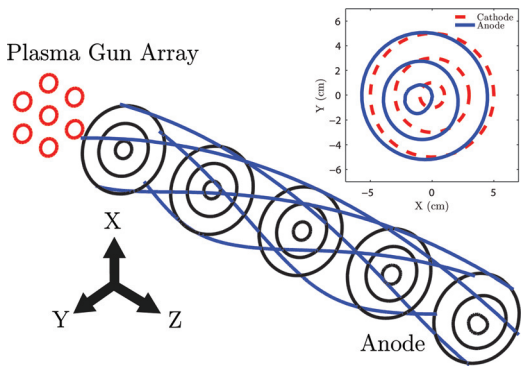

FIG. 13. (Color online) Helical equilibrium fieldline and flux surface mapping throughout the device, illustrating that circular flux surfaces are maintained. The inset illustrates the offset of the circular flux surfaces between cathode and anode, indicating that flux surfaces wander at the anode.

Furthermore, several reasons are provided to argue that the best framework for understanding the fluctuations of Sec. IV is that of a true equilibrium state. First, the exceptional coherence of all fluctuation measurements indicates that in the frame of the moving plasma there is no time dependence. Second, the equilibrium state is observed to be persistent for the entire discharge over hundreds of oscillations. Third, fieldline mapping indicates that good, circular flux surfaces are maintained throughout the plasma, as shown in Fig. 13. There is no

evidence for X-points or island-like structures in the instantaneous magnetic field. Fourth, the fluctuations exhibit both external and internal structure, indicating a truly global effect is being observed. Fifth, analysis of the perturbed radial force balance [Eq. (5)] shows that time-dependent (in the lab frame) $J \times B$ forces cause the pressure isosurfaces to rigidly displace while maintaining their structure.

It is possible that the current-driven kink instability initiates the transition from the axisymmetric to helical state. In this sense, an alternative framework for understanding the helical equilibrium of Sec. IV is that of a saturated kink. Notwithstanding, observations of the helical state onset indicate that there is no critical safety factor q at which the helical equilibrium is found, in contrast to established external kink theory.[25,26] Internal kinks, however, have no such critical q (Ref. 25), nor presumably would cases in which the distinction between internal and external kinks is inappropriate due to a poorly defined plasma boundary. Furthermore, onset as described in Sec. IV A is also consistent with a pressure-driven onset, as $P \propto I_P, B_z$, and both were found to be destabilizing. A β driven onset is not consistent with the observations, however. As the topic of pressure-driven modes in the finite length screw-pinch is largely unexplored, no comparison to theoretical predictions is attempted.

An observation of global fluctuations interpreted as a long lifetime saturated kink instability[27] exhibits several differences from the present measurements, indicating significantly different physics despite the fact that both modes were seen in linear devices utilizing similar plasma sources and exhibiting comparable flow profiles.[28] Most notably, the direction of rotation is opposite between the two modes. The long lifetime kink has been reported[27] to travel in the ion diamagnetic direction and against the $E \times B$ velocity (v_E) while the mode observed here rotates in the electron diamagnetic direction and with v_E. Some ambiguity exists, however, due to axial shear in the v_E. As shown in Fig. 10(e), the helical equilibrium may rotate against v_E for a small range of its extent. Furthermore, a theory of external kinks in the presence of axial flow[8] expects decreasing real frequency with increasing B_z while a weakly increasing scaling is observed, and the magnitude of the real frequency is underpredicted by an order of magnitude. These contrasts are likely due to the weaker role of sheath resistance and stronger role of v_E in this device.

ACKNOWLEDGMENTS

This work is supported by Department of Energy Grant No. DE-FG02-00ER54603 and National Science Foundation Grant No. 0903900. We also wish to acknowledge several individuals from the University of Wisconsin Plasma Physics Group and the Center for Magnetic Self-Organization (CMSO) who have provided their guidance, support, and time to realizing this effort.

[1]J. P. Freidberg, Rev. Mod. Phys. **54**, 801 (1982).
[2]H. Baty, Astron. Astrophys. **318**, 621 (1997).
[3]A. W. Hood, Plasma Phys. Controlled Fusion **34**, 411 (1992).
[4]E. N. Parker, Astrophys. J. **174**, 499 (1972).
[5]W. F. Bergerson, C. B. Forest, G. Fiksel, D. A. Hannum, R. Kendrick, J. S. Sarff, and S. Stambler, Phys. Rev. Lett. **96**, 015004 (2006).
[6]X. Sun, T. P. Intrator, L. Dorf, I. Furno, and G. Lapenta, Phys. Rev. Lett. **100**, 205004 (2008).
[7]I. Furno, T. P. Intrator, G. Lapenta, L. Dorf, S. Abbate, and D. D. Ryutov, Phys. Plasmas **14**, 022103 (2007).
[8]D. D. Ryutov, I. Furno, T. P. Intrator, S. Abbate, and T. Madziwa-Nussinov, Phys. Plasmas **13**, 032105 (2006).
[9]R. Lorenzini, E. Martines, P. Piovesan, D. Terranova, P. Zanca, M. Zuin, A. Alfier, D. Bonfiglio, F. Bonomo, A. Canton, S. Cappello, L. Carraro, R. Cavazzana, D. F. Escande, A. Fassina, P. Franz, M. Gobbin, P. Innocente, L. Marrelli, R. Pasqualotto, M. E. Puiatti, M. Spolaore, M. Valisa, N. Vianello, and P. Martin, Nat. Phys. **5**, 570 (2009).
[10]A. Weller, A. D. Cheetham, A. W. Edwards, R. D. Gill, A. Gondhalekar, R. S. Granetz, J. Snipes, and J. A. Wesson, Phys. Rev. Lett. **59**, 2303 (1987).
[11]J. Menard, R. Bell, E. Fredrickson, D. Gates, S. Kaye, B. LeBlanc, R. Maingi, S. Medley, W. Park, S. Sabbagh, A. Sontag, D. Stutman, K. Tritz, W. Zhu, and the NSTX Research Team, Nucl. Fusion **45**, 539 (2005).
[12]I. Chapman, M. Hua, S. Pinches, R. Akers, A. Field, J. Graves, R. Hastie, C. Michael, and the MAST Team, Nucl. Fusion **50**, 045007 (2010).
[13]S. Yoshikawa, Phys. Rev. Lett. **27**, 1772 (1971).
[14]W. A. Cooper, J. P. Graves, A. Pochelon, O. Sauter, and L. Villard, Phys. Rev. Lett. **105**, 035003 (2010)
[15]P. Bellan, *Fundamentals of Plasma Physics*, 1st ed. Cambridge University Press, Cambridge, 2006.
[16]C. Paz-Soldan, W. F. Bergerson, M. I. Brookhart, D. A. Hannum, R. Kendrick, G. Fiksel, and C. B. Forest, Rev. Sci. Instrum. **81**, 123503 (2010).
[17]G. Fiksel, A. F. Almagri, D. Craig, M. Iida, S. C. Prager, and J. S. Sarff, Plasma Sources Sci. Technol. **5**, 78 (1996).
[18]D. J. D. Hartog, D. J. Craig, G. Fiksel, and J. S. Sarff, Plasma Sources Sci. Technol. **6**, 492 (1997).
[19]D. Hannum, "Characterizing the plasma of the rotating wall machine," Ph.d. thesis University of Wisconsin-Madison, Madison, Wisconsin, 2010.
[20]R. J. Bickerton, Proc. Phys. Soc. **72**, 618 (1958).
[21]M. Kruskal and J. L. Tuck, Proc. R. Soc. London. Ser. A **245**, 222 (1958).
[22]V. Shafranov, At. Energy (Sov. J. At. Energy) **5**, 38 (1954).
[23]I. Furno, T. P. Intrator, D. D. Ryutov, S. Abbate, T. Madziwa-Nussinov, A. Light, L. Dorf, and G. Lapenta, Phys. Rev. Lett. **97**, 015002 (2006).
[24]I. Furno, T. Intrator, E. Torbert, C. Carey, M. D. Cash, J. K. Campbell, W. J. Fienup, C. A. Werley, G. A. Wurden, and G. Fiksel, Rev. Sci. Instrum. **74**, 2324 (2003).
[25]D. D. Ryutov, R. H. Cohen, and L. D. Pearlstein, Phys. Plasmas **11**, 4740 (2004).
[26]C. C. Hegna, Phys. Plasmas **11**, 4230 (2004).
[27]T. P. Intrator, I. Furno, D. D. Ryutov, G. Lapenta, L. Dorf, and X. Sun, J. Geophys. Res. **112**, 12 (2007).
[28]L. A. Dorf, T. Intrator, X. Sun, J. Hendryx, G. A. Wurden, I. Furno, and G. Lapenta, Phys. Plasmas **17**, 102101 (2010).